Noise modeling and variance stabilization of a computed radiography (CR) mammography system subject to fixed-pattern noise

Lucas R. Borges[1,*], Marco A.C. Brochi[1], Zhongwei Xu[2], Alessandro Foi[3], Marcelo A. C. Vieira[4] and Paulo M. Azevedo-Marques[1]

[1]Ribeirão Preto Medical School, University of São Paulo, Brazil
[2]Noiseless Imaging Ltd, Tampere, Finland
[3]Tampere University, Finland
[4]São Carlos School of Engineering, University of São Paulo, Brazil

* Corresponding author. E-mail: lucas.rodrigues.borges@usp.br
Address: 3900 Av. Bandeirantes, Ribeirão Preto, São Paulo, Brazil

Abstract

In this work we model the noise properties of a computed radiography (CR) mammography system by adding an extra degree of freedom to a well-established noise model, and derive a variance-stabilizing transformation (VST) to convert the signal-dependent noise into approximately signal-independent. The proposed model relies on a quadratic variance function, which considers fixed-pattern (structural), quantum and electronic noise. It also accounts for the spatial-dependency of the noise by assuming a space-variant quantum coefficient. The proposed noise model was compared against two alternative models commonly found in the literature. The first alternative model ignores the spatial-variability of the quantum noise, and the second model assumes negligible structural noise. We also derive a variance-stabilizing transformation (VST) to convert noisy observations contaminated by the proposed noise model into observations with approximately Gaussian noise and constant variance equal to one. Finally, we estimated a look-up table that can be used as an inverse transformation in denoising applications. A phantom study was conducted to validate the noise model, VST and inverse VST. The results show that the space-variant signal-dependent quadratic noise model is appropriate to describe noise in this CR mammography system (errors$<$2.0% in terms of SNR). The two alternative noise models were outperformed by the proposed model (errors as high as 14.7% and 9.4%). The designed VST was able to stabilize the noise so that it has variance approximately equal to one (errors$<$4.1%), while the two alternative models achieved errors as high as 26.9% and 18.0%, respectively. Finally, the proposed inverse transformation was capable of returning the signal to the original signal range with virtually no bias.

Keywords: noise model, computed radiography, mammography, quantum noise, structural noise, electronic noise

1 Introduction

X-ray mammography remains as the gold standard for breast cancer screening and diagnosis around the world [1]. Even though developments in the field of breast imaging enabled the clinical use of digital radiography (DR) [2, 3] and digital breast tomosynthesis (DBT) [4, 5], many countries still rely on computed radiography (CR) for breast imaging. [6–8].

In CR systems, an image plate (IP) is exposed to an X-ray beam transmitted by an object of interest (breast), positioned above the plate. After being attenuated by the object, the X-ray energy is stored in the phosphor layer of the IP, and later read by an appropriate scanner [9].

There are a number of advantages of CR systems over the previous screen-film technology, including faster image development, reusable IPs, data readiness for storage and transmission, among others. However, a number of concerns have been raised about the low image quality [10–12] and excessive radiation dose [7, 13] in CR mammography. This scenario highlights the importance of radiation dose versus image quality optimization.

In general, high dose levels are adopted in clinical practice to overcome noise. Higher dose implies higher signal-to-noise ratio due to the quantum nature of the noise. However, higher radiation dose also implies higher risks of induced cancer [14, 15]. One possible approach to reduce radiation dose and maintain acceptable image quality is to post-process the acquired images with noise suppression algorithms.

The successful removal of noise is highly dependent on the accuracy of the adopted noise model. One model commonly used in X-ray imaging relies on a quadratic variance function, which describes the structural, quantum and electronic noise sources [16, 17]. A second commonly used model assumes negligible structural noise, with an affine variance function describing the quantum and electronic noise sources [18–20].

In previous works [20, 21], our group reported the spatial-variability of the quantum noise in raw DBT and DR images. The spatial-dependency is mainly caused by the flat-fielding calibration applied to compensate non-uniformities caused by physical phenomena such as the heel effect. A modification of the affine-variance model was designed to accommodate the spatial-dependency of the quantum noise, improving the fidelity of the noise model and thus enhancing the results obtained by noise-suppression algorithms in DBT and DM images [20,21]. However, to the best of our knowledge there are no studies investigating the spatial-variability of the quantum noise in CR mammography systems.

Another important challenge of noise suppression in X-ray images arises from the signal-dependency of the noise, as most 'off-the-shelf' denoising algorithms are designed to treat signal-independent Gaussian noise. One approach to overcome this issue is to stabilize the noise variance prior to denoising using a variance stabilizing transformation (VST) [21–24]. The VST converts the signal-dependent noise into approximately Gaussian noise with a fixed variance equal to one. Even though the literature presents VSTs dedicated to specific noise models [22,25–29], to the best of our knowledge there are no VSTs available for the stabilization of variables with the quadratic-variance noise present in CR systems.

In this work we investigate the application of a space-variant quadratic-variance noise model to describe the noise in a CR mammography system. The spatial-variability of the quantum noise was added to the model to improve the fidelity of the noise description, and thus enhance the performance of algorithms that rely on the accuracy of the noise model, such as noise suppression methods. Furthermore, a new VST dedicated to the stabilization of variables with the quadratic-variance noise model was derived. The designed VST enables the noise suppression in CR images using denoising techniques originally designed to treat Gaussian signal-independent noise.

2 Theoretical Background

Through this work we consider the signal after storage by the IP and after scanning by the CR console. Thus, the noise model already includes components such as extra electronic and readout noise that could be generated by the storage and scanning procedures.

2.1 Noise model

X-ray images are often degraded by a number of noise sources, such as structural, quantum and electronic noise. The individual noise sources may be modeled by different statistical distributions, e.g., quantum noise is typically modeled by a Poisson variable. However, the energy ranges at which most X-ray systems operate allow the assumption of Gaussian-distributed noise, thanks to the central limit theorem (CLT) [30].

Even though the CLT supports the assumption of Gaussian-distributed noise, it is important to emphasize that it does not imply that the noise is independent and identically distributed (IID). In fact, most of the X-ray imaging systems require a noise model more elaborate than the IID Gaussian.

Let us consider $z_\ell(i)$ a linearized pixel of a raw CR image at spatial position $i \in \mathbb{Z}^2$. We model the linearized pixel as [17]

$$z_\ell(i) = y_\ell(i) + \sigma(i)\,\eta(i) \tag{1}$$

where y_ℓ is the expected linearized signal response, i.e. $\mathrm{E}\{z_\ell(i)\,|y_\ell(i)\} = y_\ell(i)$; σ is the standard deviation of the noise conditioned upon the signal expectation y_ℓ, i.e. $\sigma(i) = \mathrm{std}\{z_\ell(i)\,|y_\ell(i)\}$; and η is Gaussian noise with zero mean and unity variance, i.e. $\eta(i) \sim \mathcal{N}\{0, 1\}$. Details on the linearization of the pixel response are given in Section 5.

The model presented in (1), shows the standard deviation as the function σ. Depending on the noise model being adopted, σ may contain parameters that account for noise sources such as quantum and electronic. In CR mammography, due to the non-uniformity in the response of the phosphor layer of the IP, fixed-pattern noise represents a relevant part of the noise degradation and must be accounted for [16]. Moreover, the uniformity calibration periodically performed by the system to compensate issues such as the heel effect generates spatial-variability of the noise parameters [20]. Thus, here we propose the use of a space-variant signal-dependent model to describe the noise in a CR mammography system. The model is built upon the quadratic noise variance function

$$\mathrm{var}\{z_\ell(i)\,|y_\ell(i)\} = \sigma^2_{\mathrm{VSQ}}(i) = \xi_s y_\ell^2(i) + \xi_q(i)\,y_\ell(i) + \xi_e, \tag{2}$$

where σ^2_{VSQ} is the total noise variance, ξ_s, ξ_q and ξ_e are nonnegative coefficients determining the relative strength of the fixed-pattern (structural), quantum and electronic noise sources, respectively, excluding quantization effects. Note that ξ_s and ξ_e are assumed constant, while ξ_q changes with spatial position. Throughout this paper we will adopt the initials VSQ (space-Variant Signal-dependent Quadratic) to identify this noise model.

To set a benchmark, we compare our results against those obtained using two noise models commonly found in the literature. The first one features a similar quadratic variance function, with a space-invariant ξ_q [16, 17],

$$\mathrm{var}\{z_\ell(i)\,|y_\ell(i)\} = \sigma^2_{\mathrm{ISQ}}(i) = \zeta_s y_\ell^2(i) + \zeta_q y_\ell(i) + \zeta_e, \tag{3}$$

where σ^2_{ISQ} is the total noise variance, $\zeta_s = \xi_s$ determines the relative strength of the structural noise, $\zeta_e = \xi_e$ determines the relative strength of the electronic noise and ζ_q is the spatially-invariant (as opposed to ξ_q) coefficient that determines the relative strength of the quantum

noise. We will refer to this model using the initials ISQ (space-Invariant Signal-dependent Quadratic).

The second alternative model relies on the affine variance function

$$\mathrm{var}\{z_\ell(i)\,|y_\ell(i)\} = \sigma^2_{\mathrm{VSA}}(i) = \alpha(i)\,y_\ell(i) + \beta \tag{4}$$

where σ^2_{VSA} is the total noise variance, α and β are the slope and intercept of the affine function, often related to quantum and electronic noise sources, respectively. This model is adopted in a variety of imaging modalities, including digital mammography and digital breast tomosynthesis, where the structural noise is negligible compared to the quantum and electronic noise sources [18–20]. Because the structural noise plays an important role in CR systems, we anticipate that this model will perform poorly for this system. We refer to this model using the initials VSA (space-Variant Signal-dependent Affine).

2.2 Variance-Stabilizing Transformation

Variance stabilizing transformations are mathematical tools used to convert signal-dependent noise into approximately signal-independent noise. Even though VSTs can be used for non-conventional applications such as noise simulation [31,32], they are most commonly used prior to denoising. Most denoising filters are designed to treat general signal-independent Gaussian noise, thus VSTs facilitate the application of 'off-the-shelf' denoising techniques [21–24]. One widely known VST is the Anscombe Transformation [29]

$$\mathcal{A}(x) = 2\sqrt{x + \frac{3}{8}}, \tag{5}$$

which converts a Poisson-distributed random variable x, with signal-dependent variance into approximately Gaussian-distributed data with signal-independent variance equal to one.

Another well-known VST is a modification of (5), namely the Generalized Anscombe Transformation (GAT) [22]

$$\mathcal{G}(x) = \begin{cases} \frac{2}{\alpha}\sqrt{\alpha x + \alpha^2\frac{3}{8} + \beta - \alpha\mu}, & \text{if } x > -\frac{3}{8}\alpha - \frac{\beta}{\alpha} + \mu \\ 0 & \text{if } x \leq -\frac{3}{8}\alpha - \frac{\beta}{\alpha} + \mu \end{cases} \tag{6}$$

where α is the scaling of the Poisson noise, β is the variance of the Gaussian noise and μ is the mean of the Gaussian noise. This VST is dedicated to noise models such as the VSA shown in (4), with $\mu = 0$.

Extensive work has been published on the variance stabilization of variables with noise model proportional to the signal squared (y^2) [25–28]. In general, these works adopt an observation model of the the form

$$z = (1 + \nu)y, \tag{7}$$

where ν is zero-mean Gaussian noise that accounts for fluctuations on the gain of each detector element (fixed-pattern noise). For data corrupted exclusively by fixed-pattern (multiplicative) noise, such as presented above, a variance stabilization operator (namely the natural logarithm ln) is readily available

$$g = \ln\left((1 + \nu)y\right) = \ln\left(1 + \nu\right) + \ln\left(y\right), \tag{8}$$

where g is the variable with stabilized noise. However, to the best of our knowledge, there are no VSTs available in the literature to stabilize signals corrupted specifically by the VSQ noise model described in (2), where the variance is not only proportional to y^2, but also includes affine scaling by y. Thus, following the mathematical approach adopted by [25–28], we derive here a VST dedicated to the VSQ noise model and explore its application to a CR mammography system.

3 Methods & Materials

3.1 Proposed VST for the VSQ noise model

Let us consider a linearized raw pixel value z_ℓ, with variance given by (2) and expectation y_ℓ. We seek a univariate transformation $h : \mathbb{R} \to \mathbb{R}$ such that $\mathrm{var}\{h(z_\ell)\,|y_\ell\}$ is independent of $\mathrm{E}\{h(z_\ell)|y_\ell\}$ and equal to one. By means of the "delta-method" [25–28], following a first-order Taylor expansion of h in a neighborhood of $\mathrm{E}\{z_\ell|y_\ell\} = y_\ell$, $h(z_\ell) \approx h(y_\ell) + h'(y_\ell)\,(z_\ell - y_\ell)$, the variance $\mathrm{var}\{h(z_\ell)\,|y_\ell\}$ of the transformed z_ℓ can be described as

$$\mathrm{var}\{h(z_\ell)\,|y_\ell\} \approx \left(h'(y_\ell)\right)^2 \mathrm{var}\{z_\ell|y_\ell\}\,, \tag{9}$$

where h' denotes the first derivative of h. As our goal is to obtain $\mathrm{var}\{h(z_\ell)\,|y_\ell\} = 1$, we want h to satisfy

$$h'(y_\ell) = \frac{1}{\mathrm{std}\{z_\ell|y_\ell\}}\,, \tag{10}$$

which is solved by having h to be the primitive function of the reciprocal of $\mathrm{std}\{z_\ell|y_\ell\}$.

We know from (2) that $\mathrm{std}\{z_\ell|y_\ell\} = \sqrt{\xi_s y_\ell^2 + \xi_q y_\ell + \xi_e}$ and thus, after tedious computations, we obtain

$$h\left(z_\ell\right) = \frac{\ln\left(\left|2\sqrt{\xi_s}\sqrt{\xi_s z_\ell^2 + \xi_q z_\ell + \xi_e} + 2\xi_s z_\ell + \xi_q\right|\right)}{\sqrt{\xi_s}}. \tag{11}$$

Note that through (9)–(11) the spatial coordinate i was omitted to improve clarity. As mentioned above, a simple first-order approximation was adopted. This assumption will impact the accuracy of the stabilized variance, especially at low counts. Details are discussed later in Section 6.

3.2 Inverse Transformation

One of the important aspects of using VSTs is to choose the appropriate inverse transformation. Because the VSTs are generally non-linear transformations, modifications on the signal in the VST range may cause bias in the signal if the inverse transformation is not designed properly. This issue has been studied in depth in previous works [33, 34].

Let us consider $\mathcal{F}$ as the forward variance-stabilizing transformation. We seek an inverse transformation $\mathcal{I}$ such that

$$\mathcal{I} : \mathrm{E}\{\mathcal{F}\left(z_\ell\right)|y_\ell\} \longmapsto \mathrm{E}\{z_\ell|y_\ell\}. \tag{12}$$

Different approaches may be adopted to compute the inverse $\mathcal{I}$. To that end, both $\mathrm{E}\{z_\ell|y_\ell\}$ and $\mathrm{E}\{\mathcal{F}\left(z_\ell\right)|y_\ell\}$ must be first computed. Trivially, $\mathrm{E}\{z_\ell|y_\ell\} = y_\ell$, and $\mathrm{E}\{\mathcal{F}\left(z_\ell\right)|y_\ell\}$ can be computed using, e.g., numerical integration such as in [34], or using Monte-Carlo sampling.

3.3 Image Dataset

All images in this study were acquired at the Clinics Hospital of the Ribeirão Preto Medical School (Brazil), using a clinical setup featuring the Mammomat 3000 Nova (Siemens), manufactured in 2009, the DirectView CR scanner (Carestream), manufactured in 2010, and a CR mammography cassette with an EHR-MS3 screen (Carestream), manufactured in 2017. The cassete was randomly selected and has a pixel size of 48.5μm.

A 3.5cm thick uniform polymethyl methacrylate (PMMA) phantom was used in the experiments. The uniform PMMA block is commonly used for the periodic flat-fielding calibration

as it allows an easy estimation of the signal and noise properties. The phantom was positioned directly over the detector plate and covered the entire detector field. Only raw data was analyzed.

The system was first set to automatic mode (AEC) with selected tube voltage of 28 kVp, and Mo/Rh target/filter combination. The resulting current-time product was 86 mAs. Next, the system was set to manual mode, with 28 kVp, Mo/Rh target/filter combination and current-time products of 22, 45, 63, 90, 110 and 200 mAs. Two realizations were acquired at each mAs selected manually. The different mAs were adopted to represent a range of dose levels, and thus a range of SNR regimes.

4 Experiments

4.1 Estimation of local expectation and local variance

Throughout this work, the local signal expectation and local noise variance were estimated in several occasions. To estimate the expectation and variance maps, we started by cropping approximately 20mm from the top and bottom and approximately 10mm from the left and right borders of the raw images. This was done to remove annotations and dead pixels from the borders.

The local expected signal, at a spatial coordinate i, was estimated using the average over a 1.7mm $\times$ 1.7mm sliding window centered at i. Before estimating the noise variance, the realization was detrended by subtracting the estimated signal expectation from the observed signal. The local variance at a spatial coordinate i was then estimated as the square of the sample standard deviation over a 1.7mm $\times$ 1.7mm sliding window centered at i.

As we have access to two realizations of each imaging configuration, we conducted the procedures described above on both realizations. To investigate the repeatability of the measurements we reported in the results section the average variability between the two acquisitions. The final results were reported as the average among the two measurements.

4.2 Estimation of space-invariant noise coefficients

To estimate the space-invariant noise coefficients ξ_s, ξ_e, ζ_s, ζ_q, ζ_e and β, a 20 mm $\times$ 20 mm ROI was taken from the center of each realization at each dose. A small ROI was chosen to minimize possible variations of ξ_q and β.

The local signal expectation and local noise variance were estimated from each ROI using the procedure described in 4.1. The relationship between the average expectation vs. the average variance over the ROI was fitted using a second order polynomial regression, in the the case of ξ_s, ξ_e, ζ_s, ζ_q and ζ_e, and a first order polynomial regression in the case of β.

4.3 Estimation of space-variant noise coefficients

The coefficients $\xi_q(i)$ were estimated using the space-invariant ξ_s and ξ_e, estimated through the procedure described in Subsection 4.2; the local signal y_ℓ and local variance σ^2_{VSQ}, estimated through the procedure described in Subsection 4.1; and the relation derived from (2)

$$\xi_q(i) = \frac{\sigma^2_{\text{VSQ}}(i) - \xi_s\, y^2(i) - \xi_e}{y_\ell(i)}. \tag{13}$$

A second-order polynomial surface was fitted to the estimated ξ_q to minimize variations due to the limited number of realizations. A similar procedure was used to estimate $\alpha(i)$. Details on the estimation of $\alpha(i)$ are given in [20].

4.4 Theoretical Signal-to-noise Ratio

The accuracies of the noise models were investigated using the local signal-to-noise ratio (SNR). The SNR was estimated and compared against the theoretical SNR dictated by the noise models (2)–(4)

$$SNR_{\text{VSQ}}(i) = \frac{y_\ell(i)}{\sqrt{\xi_s y_\ell^2(i) + \xi_q(i)\, y_\ell(i) + \xi_e}} \quad , \tag{14}$$

$$SNR_{\text{ISQ}}(i) = \frac{y_\ell(i)}{\sqrt{\zeta_s y_\ell^2(i) + \zeta_q y_\ell(i) + \zeta_e}} \quad , \tag{15}$$

$$SNR_{\text{VSA}}(i) = \frac{y_\ell(i)}{\sqrt{\alpha(i)\, y_\ell(i) + \beta}} \quad , \tag{16}$$

where SNR_{VSQ}, SNR_{ISQ} and SNR_{VSA} are the local SNR maps predicted by the VSQ, ISQ and VSA noise models, respectively. The experimental SNR was estimated as the ratio between the expectation and standard deviation of the signal, both estimated following the procedures presented in Section 4.1.

The overall performance of the models was estimated using the pointwise relative error between the SNR values predicted by the theoretical models (14)–(16) and the values measured from clinical data. The error map between two quantities a and $\hat{a}$ was estimated as the relative difference $\varepsilon_{a,\hat{a}}(i) = |a(i) - \hat{a}(i)|/a(i)$. Boxplots of the error maps were reported, as they allow the visualization of the error's median, minimum, maximum, 25th percentile and 75th percentile.

5 Results

As most CR systems, the equipment used in this work reports logarithmic response to X-ray exposure. Thus, the first step in all experiments was to linearize the detector response. This was achieved by fitting an exponential function f_l such that $z_\ell = f_l(z) = \gamma$, where γ is the current-time product, in mAs, at which the uniform image was acquired [35], z is the observed pixel and z_ℓ is the linearized observed pixel.

Figure 1 shows the pixel values before and after linearization, as a function of the current-time product (mAs). Because the signal before and after linearization belong to different ranges, Figure 1 reports two y-axis scales – the left one shows the range before linearization, and on the right is the signal range after linearization.

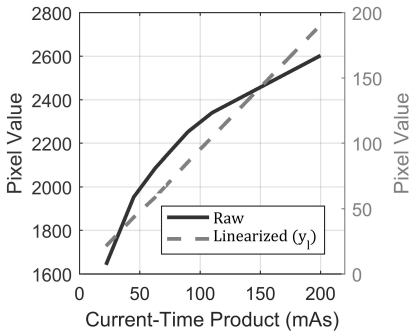

Figure 1: Detector response before and after the linearization process. The scale on the left axis represents the pixel range before linearization, and the right axis after linearization.

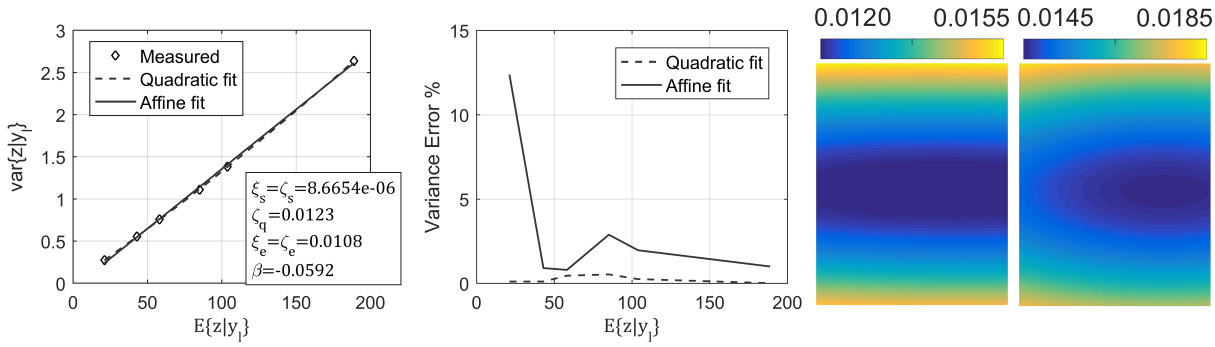

(a) (b) (c) (d)

Figure 2: Coefficient estimation. (a) Variance versus expectation plot for the estimation of spatial-invariant coefficients. (b) Fitting errors of the quadratic and affine fits. (c) and (d) Maps illustrating the spatial-variant parameters ξ_q and α, respectively.

5.1 Noise Coefficients

Figure 2 shows the results of the coefficient estimation. In Figure 2 (a), the variance versus expectation relationship was fitted using a first and a second order polynomial. Figure 2 (b) shows the relative errors between measured and fitted variances, calculated as the percentage difference. Figures 2 (c) and (d) show the estimated ξ_q and α maps, respectively.

5.2 Signal-to-noise Ratio

The estimated local signal expectation and local noise variance were used to calculate the local SNR at each dose level. To minimize variations due to the low number of acquisitions, second order polynomial surfaces were fitted to each estimated variance map.

Using the estimated signal expectation, estimated noise coefficients and equations (14)–(16), we also calculated the theoretical SNR maps predicted by each noise model. Figure 3 shows examples of the theoretical and measured SNR maps at 22 and 200 mAs. Figure 4 (top) shows the SNR measured at each mAs. From the boxplots, it is possible to appreciate the median, maximum, minimum, 25th and 75th percentiles of the theoretical SNRs. The horizontal dotted lines represents the median of the experimental SNR at each mAs, estimated using the phantom data. Figure 4 (bottom) shows the errors between measured and calculated SNR maps.

The average SNR variability among two realizations at the same dose was 0.5%, with standard deviation of 0.7%.

5.3 Variance Stabilization

The transformation proposed in (11) was applied to the linearized images, considering the proposed VSQ and ISQ noise models, and the respective estimated noise coefficientes. The GAT, described in (6), was also applied considering the VSA model and the respective estimated noise coefficients.

To evaluate the performance of each VST, the local noise variance was estimated. Figure 5 shows examples of the variance maps before and after stabilization at 22 and 200 mAs. Figure 6 (top) shows the boxplots of the local stabilized variance from each mAs and noise model. Figure 6 (bottom) shows the error in the stabilized variance for each model.

The average variance variability among two realizations at the same dose was 1.7%, with standard deviation of 2.2%.

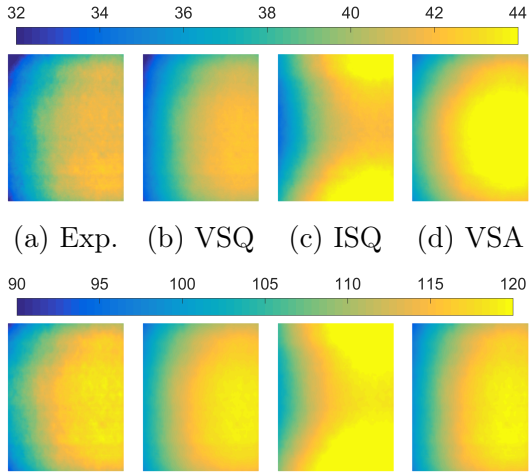

(a) Exp. (b) VSQ (c) ISQ (d) VSA

(e) Exp. (f) VSQ (g) ISQ (h) VSA

Figure 3: Experimental versus predicted SNR maps at two dose levels. Top row: 22 mAs, bottom row: 200 mAs. Columns from the left: experimental data, VSQ (14), ISQ (15) and VSA (16) noise models.

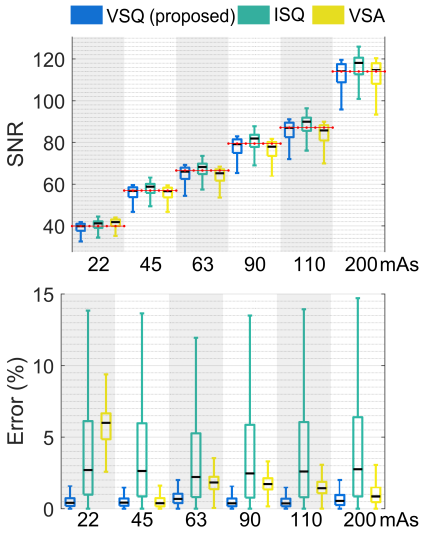

Figure 4: SNR evaluation. Top: SNR measurements. Bottom: Average pointwise relative error between experimental and theoretical SNR. The boxplots report the median, 25th, 75th percentiles, the maximum and minimum values, excluding outliers [36]. Red lines represent the measured values.

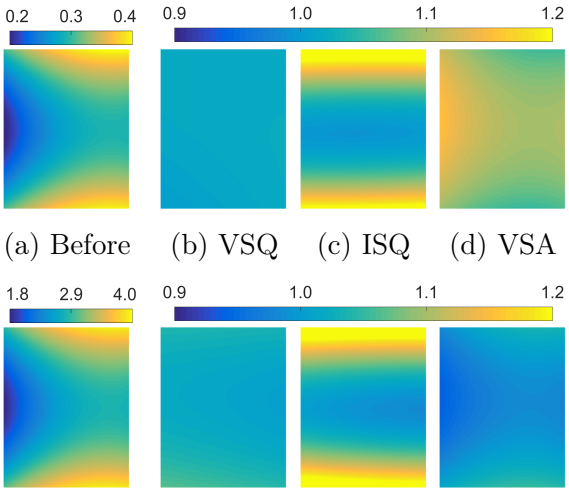

(a) Before (b) VSQ (c) ISQ (d) VSA

(e) Before (f) VSQ (g) ISQ (h) VSA

Figure 5: Variance maps. Top: 22 mAs, bottom: 200 mAs. First column to the left: variance before VST. Remaining columns: variance after VST considering the VSQ (2), ISQ (3) and VSA (4) noise models, respectively.

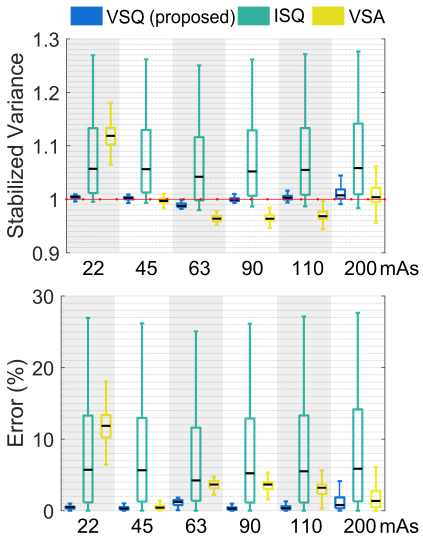

Figure 6: Evaluating the accuracy and precision in the stabilization of variance under different models. Top: Variance measurements. Bottom: Average pointwise relative error between estabilized variance and target variance (1). The boxplots report the median, 25th, 75th percentiles, the maximum and minimum values, excluding outliers [36].

5.4 Inverse Transformation

To obtain an approximation of the inverse transformation, we conducted a Monte Carlo numerical simulation, with 10^3 equally spaced y_ℓ values taken from 20 to 200, and 10^3 equally spaced ξ_q ranging from 0.0113 to 0.0150, simulating the values obtained in our clinical dataset. Observations z_ℓ were simulated by adding noise to y_ℓ using the model described in (2). The experiment used 10^4 realizations of z_ℓ.

The VST was applied to the noisy simulated data, and an estimation of $\mathrm{E}\{\mathcal{F}(z)\,|y_\ell\}$ was obtained by numerical integration among the realizations. A look-up table was then created using the signal in the VST domain and the coefficient ξ_q as input, and the ground-truth signal y_ℓ at the spatial range as the output. Although there are other possible ways to design the inverse VST, such as defining a closed-form analytical approximation, we opted to use a look-up table due to the precision achieved by this method, and the readiness of the resulting data - since the values are already pre-computed and saved, it is enough to simply load the data and use it. Intermediate values not present in the table can be estimated using a first-order 2D interpolation. Figure 7 shows examples of $\mathcal{I}$ at three different ξ_q values.

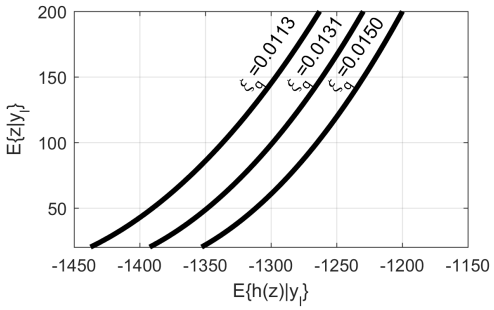

Figure 7: Examples of the inverse transformation $\mathcal{I}$ for three values of ξ_q.

6 Discussion

In this work we investigated the noise characteristics of a CR mammography system, and proposed a variance stabilizing transformation as well as its corresponding inverse transformation.

First, noise coefficients were estimated considering three scenarios: a space-variant quadratic variance model, described in (2); a space-invariant quadratic variance model, described in (3); and a space-variant affine variance model, described in (4). The estimated coefficients were reported in Figure 2. Even though ξ_s is in the order of 10^{-6}, this coefficient is related to the signal squared, and thus its contribution is relevant to the noise modeling, as made evident later in the SNR analysis shown in Figures 3 and 4.

In Figures 3 (c) and (g), the SNR maps show that, even though the range of SNR values predicted by the ISQ model is close to the measured, the spatial distribution of the SNR is considerably different from the measurements shown in Figures 3 (a) and (e). This behavior is explained by the lack of spatial-variability of the quantum noise coefficient.

Figures 3 (d) and (h) show that, even though the VSA model was able to reproduce the measured SNR with high fidelity at 200 mAs, the predicted SNR is considerably higher than the expected at 22mAs. In this case, assuming negligible structural noise caused errors in different doses, but the spatial-variability is preserved thanks to the spatially-dependent variable $\alpha(i)$.

Figure 4 shows that the proposed noise model achieved errors smaller than 2.0%, while the ISQ and VSA models reported errors up to 14.7% and 9.4%, respectively.

Figures 5 and 6 show that the proposed variance stabilizing transformation, used in conjunction with the proposed noise model, was able to stabilize the noise variance to one. Carefull

analysis of the boxplot presented in Figure 6 (bottom) shows that the highest error achieved by the VSQ model was 4.1% at 200mAs, while the ISQ and VSA model used in conjunction with the proposed VST and GAT, respectively, reported considerably larger errors (26.9% and 18.0%, respectively).

The proposed VST relies on a simple first order approximation. Even though the proposed function is able to stabilize the variance at the pixel range considered in this work, errors may arise as the pixel values decrease. For a better approximation of the transformation, a careful analysis of the Taylor expansion of this function is required.

Examples taken from the look-up table are shown in Figure 7. It is important to highlight that the look-up table was designed to perform the inverse transformation within the range of coefficients and pixel values at which this system operates. If applied to signals outside these ranges the behaviour of the inverse transformation is difficult to predict and may cause large signal bias.

The validation presented in this work was performed using a single imaging plate. However, some variability is expected in the noise parameters among different IPs or as the IP ages. Thus, a more detailed study is required for any claims about the extrapolation of the estimated parameters to other IPs of the same model or to the same IP at different time points.

Even though in this work we focused on mammography CR, the VST derived here is applicable to other imaging modalities and other CR imaging systems that share similar quadratic variance noise model.

7 Conclusion

The space-variant quadratic model was sufficient to accurately describe the noise variance of the CR mammography system. The proposed variance stabilizing transformation was able to stabilize the variance of the noise model found in this CR mammography system.

Acknowledgements

This work was supported by the São Paulo Research Foundation (FAPESP 2018/19888-5 and INCT2014 14/50889-7) and the Academy of Finland (project no. 310779).

References

[1] A. Karellas and S. Vedantham, "Breast cancer imaging: a perspective for the next decade," *Medical Physics*, vol. 35, no. 11, pp. 4878–4897, 2008.

[2] J. M. Lewin, R. E. Hendrick, C. J. D'Orsi, P. K. Isaacs, L. J. Moss, A. Karellas, G. A. Sisney, C. C. Kuni, and G. R. Cutter, "Comparison of full-field digital mammography with screen-film mammography for cancer detection: results of 4,945 paired examinations," *Radiology*, vol. 218, no. 3, pp. 873–880, 2001.

[3] E. D. Pisano, C. Gatsonis, E. Hendrick, M. Yaffe, J. K. Baum, S. Acharyya, E. F. Conant, L. L. Fajardo, L. Bassett, C. D'orsi *et al.*, "Diagnostic performance of digital versus film mammography for breast-cancer screening," *New England Journal of Medicine*, vol. 353, no. 17, pp. 1773–1783, 2005.

[4] L. T. Niklason, B. T. Christian, L. E. Niklason, D. B. Kopans, D. E. Castleberry, B. Opsahl-Ong, C. E. Landberg, P. J. Slanetz, A. A. Giardino, R. Moore *et al.*, "Digital tomosynthesis in breast imaging." *Radiology*, vol. 205, no. 2, pp. 399–406, 1997.

[5] S. M. Friedewald, E. A. Rafferty, S. L. Rose, M. A. Durand, D. M. Plecha, J. S. Greenberg, M. K. Hayes, D. S. Copit, K. L. Carlson, T. M. Cink *et al.*, "Breast cancer screening using tomosynthesis in combination with digital mammography," *JAMA*, vol. 311, no. 24, pp. 2499–2507, 2014.

[6] S. Hong, S. Y. Song, B. Park, M. Suh, K. S. Choi, S. E. Jung, M. J. Kim, E. H. Lee, C. W. Lee, and J. K. Jun, "Effect of digital mammography for breast cancer screening: A comparative study of more than 8 million korean women," *Radiology*, vol. 294, no. 2, pp. 247–255, 2020.

[7] B. Barufaldi, S. P. Zuckerman, R. B. Medeiros, A. D. Maidment, and H. Schiabel, "Characterization of the imaging settings in screening mammography using a tracking and reporting system: A multi-center and multi-vendor analysis," *Physica Medica*, vol. 71, pp. 137–149, 2020.

[8] M.-E. Brandan, C. Ruiz-Trejo, N. Cansino, J.-C. C. Hernández, A. Moreno-Ramírez, J. A. Rodriguez-López, E. López-Pineda, M. Gómez-Zepeda, and M. Chevalier, "Overall performance, image quality, and dose, in computed radiology (CR) mammography systems operating in the mexican public sector," in *15th International Workshop on Breast Imaging (IWBI2020)*, vol. 11513. International Society for Optics and Photonics, 2020, p. 115131J.

[9] M. Sonoda, M. Takano, J. Miyahara, and H. Kato, "Computed radiography utilizing scanning laser stimulated luminescence." *Radiology*, vol. 148, no. 3, pp. 833–838, 1983.

[10] X. J. Rong, C. C. Shaw, D. A. Johnston, M. R. Lemacks, X. Liu, G. J. Whitman, M. J. Dryden, T. W. Stephens, S. K. Thompson, K. T. Krugh *et al.*, "Microcalcification detectability for four mammographic detectors: Flat-panel, CCD, CR, and screen/film," *Medical Physics*, vol. 29, no. 9, pp. 2052–2061, 2002.

[11] P. Monnin, D. Gutierrez, S. Bulling, D. Lepori, J.-F. Valley, and F. Verdun, "Performance comparison of an active matrix flat panel imager, computed radiography system, and a screen-film system at four standard radiation qualities," *Medical Physics*, vol. 32, no. 2, pp. 343–350, 2005.

[12] J. Fernandez, J. Ordiales, E. Guibelalde, C. Prieto, and E. Vano, "Physical image quality comparison of four types of digital detector for chest radiology," *Radiation protection dosimetry*, vol. 129, no. 1-3, pp. 140–143, 2008.

[13] J. E. Aldrich, E. Duran, P. Dunlop, and J. R. Mayo, "Optimization of dose and image quality for computed radiography and digital radiography," *Journal of Digital Imaging*, vol. 19, no. 2, pp. 126–131, 2006.

[14] A. B. de Gonzalez, C. D. Berg, K. Visvanathan, and M. Robson, "Estimated risk of radiation-induced breast cancer from mammographic screening for young BRCA mutation carriers," *Journal of the National Cancer Institute*, vol. 101, no. 3, pp. 205–209, 2009.

[15] M. J. Yaffe and J. G. Mainprize, "Risk of radiation-induced breast cancer from mammographic screening," *Radiology*, vol. 258, no. 1, pp. 98–105, 2011.

[16] A. Burgess, "On the noise variance of a digital mammography system," *Medical Physics*, vol. 31, no. 7, pp. 1987–1995, 2004.

[17] N. Marshall, P. Monnin, H. Bosmans, F. Bochud, and F. Verdun, "Image quality assessment in digital mammography: Part I. Technical characterization of the systems," *Physics in Medicine & Biology*, vol. 56, no. 14, p. 4201, 2011.

[18] P. Gravel, G. Beaudoin, and J. A. De Guise, "A method for modeling noise in medical images," *IEEE Transactions on Medical Imaging*, vol. 23, no. 10, pp. 1221–1232, 2004.

[19] A. Manduca, L. Yu, J. D. Trzasko, N. Khaylova, J. M. Kofler, C. M. McCollough, and J. G. Fletcher, "Projection space denoising with bilateral filtering and CT noise modeling for dose reduction in CT," *Medical Physics*, vol. 36, no. 11, pp. 4911–4919, 2009.

[20] L. R. Borges, L. Azzari, P. R. Bakic, A. D. Maidment, M. A. Vieira, and A. Foi, "Restoration of low-dose digital breast tomosynthesis," *Measurement Science and Technology*, vol. 29, no. 6, p. 064003, 2018.

[21] L. R. Borges, P. R. Bakic, A. Foi, A. D. Maidment, and M. A. Vieira, "Pipeline for effective denoising of digital mammography and digital breast tomosynthesis," in *Medical Imaging 2017: Physics of Medical Imaging*, vol. 10132. International Society for Optics and Photonics, 2017, p. 1013206.

[22] J.-L. Starck, F. D. Murtagh, and A. Bijaoui, *Image processing and data analysis: the multiscale approach*. Cambridge University Press, 1998.

[23] S. H. Chan, O. A. Elgendy, and X. Wang, "Images from bits: Non-iterative image reconstruction for quanta image sensors," *Sensors*, vol. 16, no. 11, p. 1961, 2016.

[24] L. Azzari and A. Foi, "Variance stabilization for noisy+ estimate combination in iterative Poisson denoising," *IEEE Signal Processing Letters*, vol. 23, no. 8, pp. 1086–1090, 2016.

[25] P. R. Prucnal and B. E. Saleh, "Transformation of image-signal-dependent noise into image-signal-independent noise," *Optics Letters*, vol. 6, no. 7, pp. 316–318, 1981.

[26] H. Arsenault and M. Denis, "Integral expression for transforming signal-dependent noise into signal-independent noise," *Optics Letters*, vol. 6, no. 5, pp. 210–212, 1981.

[27] H. Arsenault and G. April, "Properties of speckle integrated with a finite aperture and logarithmically transformed," *JOSA*, vol. 66, no. 11, pp. 1160–1163, 1976.

[28] H. Arsenault, C. Gendron, and M. Denis, "Transformation of film-grain noise into signal-independent additive Gaussian noise," *JOSA*, vol. 71, no. 1, pp. 91–94, 1981.

[29] F. J. Anscombe, "The transformation of Poisson, binomial and negative-binomial data," *Biometrika*, vol. 35, no. 3/4, pp. 246–254, 1948. [Online]. Available: http://www.jstor.org/stable/2332343

[30] A. Papoulis and S. U. Pillai, *Probability, random variables, and stochastic processes*. Tata McGraw-Hill Education, 2002.

[31] L. R. Borges, H. C. Oliveira, P. F. Nunes, P. R. Bakic, A. D. A. Maidment, and M. A. C. Vieira, "Method for simulating dose reduction in digital mammography using the Anscombe transformation," *Medical Physics*, vol. 43, no. 6, pp. 2704–2714, 2016.

[32] L. R. Borges, I. Guerrero, P. R. Bakic, A. Foi, A. D. Maidment, and M. A. Vieira, "Method for simulating dose reduction in digital breast tomosynthesis," *IEEE Transactions on Medical Imaging*, vol. 36, no. 11, pp. 2331–2342, 2017.

[33] M. Makitalo and A. Foi, "Optimal inversion of the Anscombe transformation in low-count Poisson image denoising," *IEEE Transactions on Image Processing*, vol. 20, no. 1, pp. 99–109, 2011.

[34] ——, "Optimal inversion of the generalized Anscombe transformation for Poisson-Gaussian noise," *IEEE Transactions on Image Processing*, vol. 22, no. 1, pp. 91–103, 2013.

[35] K. Young, J. Oduko, H. Bosmans, K. Nijs, and L. Martinez, "Optimal beam quality selection in digital mammography," *The British Journal of Radiology*, vol. 79, no. 948, pp. 981–990, 2006.

[36] M. Frigge, D. C. Hoaglin, and B. Iglewicz, "Some implementations of the boxplot," *The American Statistician*, vol. 43, no. 1, pp. 50–54, 1989.